ORNL/LTR-2022/2543

Evaluation of the Feasibility of Utilizing a Low-Cost UWB Radar for Hardware Implant & Counterfeit Device Detection

Corey D. Cooke
Kyle Reed
Tristen Mullins
Lance Wetzel
Timothy Daniel
Lauren Torkelson
Gregory Sheets
Juan Lopez, Jr.

January 2023

OAK RIDGE National Laboratory

ORNL IS MANAGED BY UT-BATTELLE LLC FOR THE US DEPARTMENT OF ENERGY

ORNL/LTR-2022/2543

Cyber Resilience & Intelligence Division

EVALUATION OF THE FEASIBILITY OF UTILIZING A LOW-COST UWB RADAR FOR HARDWARE IMPLANT & COUNTERFEIT DEVICE DETECTION

Corey D. Cooke
Kyle Reed
Tristen Mullins
Lance Wetzel
Timothy Daniel
Lauren Torkelson
Gregory Sheets
Juan Lopez, Jr.

January 2023

Prepared by
OAK RIDGE NATIONAL LABORATORY
Oak Ridge, TN 37831
managed by
UT-Battelle LLC
for the
US DEPARTMENT OF ENERGY
under contract DE-AC05-00OR22725

ABSTRACT

Hardware implants & counterfeit devices in the US power grid pose a significant national security threat. Asset owners currently have few options for detecting the presence of such devices "in the wild". The goal of this work is to develop a non-invasive sensing method to solve this problem. In this work we evaluate the feasibility of implementing a nonlinear UWB radar tomography system to differentiate between electronic internals of externally-similar devices using low-cost off-the-shelf hardware.

1 INTRODUCTION

According to the Office of the Director of National Intelligence (ODNI), supply chain exploitation, especially when executed as a blended operation in concert with cyber intrusions, malicious insiders, and economic espionage, threatens the U.S. critical infrastructure [1]. Supply chain risks may include insertion of counterfeits, unauthorized production, tampering, theft, insertion of malicious software and hardware, as well as poor manufacturing and development practices in the Information and Communications Technology (ICT) supply chain [2].

Prior research activities have focused on securing the supply chain during pre-acquisition and acquisition activities [3–13]. In this work, we propose a novel application of ultra-wideband (UWB) radar technology to provide the capability to start addressing the aforementioned supply chain threats at the asset owner level (end of the supply chain) where the threat materializes and has a measurable impact. We propose the combination of UWB radar with tomographic imaging of nonlinear backscatter to create a non-invasive sensor that can discriminate between electronic devices that have external similarity. In particular, our focus is on determining the presence of counterfeits and/or hardware implants in industrial control and bulk power system equipment.

1.1 Literature Review

The nonlinear nature of electronic components allows them to be differentiated from metal and/or dielectric enclosures which generally have a linear response. Prior work has shown that even small differences in nonlinear electronic components (such as power supplies) can produce detectable differences in emissions [14, 15].

Several authors have used radars to illuminate a target and measure the backscatter from the nonlinear components. Mazzaro gives a good overview of the topic, termed "harmonic radar" [16]. A variety of waveforms are used for detecting the presence of electronics [17–21]. The objective of such systems vary from simple detection of radio transceivers [22, 23] to producing images of specified areas [24, 25]. Harmonic radars generally attempt to detect whether in-band intermodulation products (IMOD) (e.g. [21]) or out-of-band (OOB) harmonics (e.g. [26]). OOB radiation is simpler to discriminate in the frequency domain, but imposes extra hardware requirements on the RX antenna and receiver hardware. IMOD approaches have simpler hardware requirements, but may require more sophisticated signal processing to separate the linear response (which is generally regarded as clutter) from the nonlinear response. Most of the systems cited in this section use one or more continuous wave (CW) or pulsed frequency-modulated (FM) waveforms; these are generally straightforward to generate at a desired power level.

1.2 Proposed Approach

For imaging the internals of an ICT device, certain additional constraints are imposed that may make prior approaches infeasible. First, the proposed sensor must comply with FCC spectral regulations. Secondly, a small form factor is desirable so that a technican can hand-carry the device. Lastly, a low transmit power is required so as not to present a health and safety risk to the technician or nearby equipment. Due to the low power requirement, such a sensor will have a very short range (1-2 meters). At these ranges, CW or FM waveforms, particularly when using pulse compression, are infeasible due to excessive isolation requirements between TX and RX.

Impulse radio ultra-wideband (IR-UWB) radar is one promising solution that meets these requirements [27]. Instead of modulating a carrier to achieve wide bandwidths, IR-UWB uses short pulses (on the order of nanoseconds); this avoids the isolation problem at short ranges, but has the downside that pulse energy is generally much lower. UWB systems have been approved by the FCC for use in the US in the 3.1 to 10.6 GHz band, provided that the power spectral density is less than -41.3 dBm/MHz. However, such devices generally have highly specialized front-ends, meaning that OOB harmonic approaches are ruled out.

1.3 Original Contributions

UWB IMOD tomography has been reported in the literature previously [28, 29]. However, in this work, the targets imaged were very simple (e.g. a single diode embedded in a dielectric block) and the method was not applied to complex electronic systems. As well, the objective of this prior work appeared to be simple *detection* and *localization* of electronic devices, whereas the objective of this work is *differentiation* between devices that appear outwardly similar.

Another original contribution of this work is the development of a system that complies with FCC spectral and power requirements. This means that the device will be safe for a technician to use and will not cause excessive harmful interference with other neighboring systems. These constraints created nontrivial engineering challenges that had to be solved for the system be able to function, largely due to the very low power levels involved.

Lastly, the use of machine learning (ML) to differentiate between similar complex nonlinear scattering patterns generated by UWB tomography is a novel advancement. As was previously mentioned, most prior work appears to be focused on detection and localization rather than differentiation. The final paper will present the results of applying our ML classifier to actual measurement data.

In this work we will demonstrate the imaging algorithms using a software phantoms, a technique common in medical imaging literature. We are in the process of building an anechoic chamber; when this facility is complete we will be able to validate these algorithms on real hardware and targets and report the results in the full version of this paper.

2 METHODOLOGY

2.1 System Description

Additional detail about the system will be described below. The P440 radar has a maximum EIRP of -13 dBm and a pulse repetition frequency (PRF) of 10 MHz. Three Vivaldi directional UWB antennas with approximately 11 dBi gain are used in the system. For device characterization, the DUT is placed on a free-space dielectric turntable that is angle-controllable. The backscattered return is passed through a 5.8 GHz notch filter to remove both the direct and backscattered illuminator signal, which is necessary because the illuminator is several orders of magnitude stronger than the UWB signal. Because the signal features of interest will be very weak, large coherent processing intervals (CPIs) will be needed.

The coherently integrated received voltage as a function of delay was collected for several aspect angles. For each aspect angle, the target is illuminated with N pulses with the illuminator present, and N pulses without the illuminator present, where N is the CPI. The contrast signal is then generated by subtracting the "illuminator + pulse" return from the "pulse only" return. Because the illuminator signal is filtered out with the notch + BPF, the contrast signal contains only the intermodulation products. The inverse Radon transform [30] was performed on the contrast data to generate a 2D image of the internals of the object with the clutter removed.

2.2 Intermodulation Tomography

2.2.1 Nonlinear Scattering Model

In this section we will describe a behavioral circuit model of the nonlinear electronic components. If we model the internal electronic components as memoryless nonlinearities, we can express the output signal as a Taylor polynomial function of the input [31]:

$$v(x) = c_1 x + c_2 x^2 + c_3 x^3 \ldots . \tag{1}$$

We only need concern ourselves with the signal components near f_c. For this reason, the even-power terms will fall OOB and can be neglected. For small input signal power levels, the higher-order terms will be similarly weak; as a result we will approximate the output as follows:

$$v(x) \approx c_1 x + c_3 x^3. \tag{2}$$

If the UWB pulse is $x_1(t) = a_1 \cos(\theta_1(t))$ and the illuminator is $x_2(t) = a_2 \cos(\theta_2(t))$, where $\theta_i(t) = 2\pi f_i t + \phi_i(t)$, the system output is (with OOB terms omitted):

$$v(x_1 + x_2) \approx a_1 \cos\theta_1 \left[c_1 + c_3 \left(\frac{3}{4} a_1^2 + \frac{3}{2} a_2^2 \right) \right] + \frac{3}{2} c_3 a_1^2 a_2 \cos\theta_2 + \frac{3}{4} c_3 a_1^2 a_2 \cos(2\theta_1 - \theta_2). \tag{3}$$

Because $|a_2| \gg |a_1|$, we can simplify:

$$v(x_1 + x_2) \approx a_1 \cos\theta_1 \left[\underbrace{c_1}_{\text{Linear}} + \underbrace{\frac{3}{2} c_3 a_2^2}_{\text{In-band IMOD}} \right] + \underbrace{\frac{3}{2} c_3 a_1^2 a_2 \cos\theta_2}_{\text{Hi-band IMOD}} + \underbrace{\frac{3}{4} c_3 a_1^2 a_2 \cos(2\theta_1 - \theta_2)}_{\text{Lo-band IMOD}}. \tag{4}$$

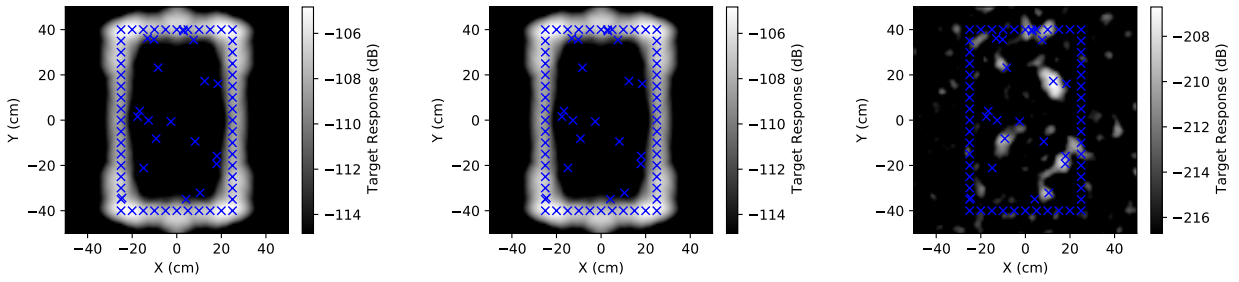

(a) Pulse only. **(b) Pulse + illuminator.** **(c) Contrast.**

Figure 1. Tomography images generated from 1U rack mount phantom. Scatterer locations are marked with ×. Note that the contrast image shows approximate locations of the nonlinear scatterers, and the linear clutter has been largely removed.

Assuming that the Hi-band and Lo-band IMOD terms are small relative to the in-band terms, we can define an equivalent linear and nonlinear radar cross-section (RCS) for each scatterer as follows:

$$\sigma_{\text{linear}} = \frac{\lambda}{4\pi} G_r G_t c_1^2, \tag{5}$$

where G_r and G_r are the equivalent scatterer antenna gains and c_1 is the linear gain from (4), and the nonlinear RCS is:

$$\sigma_{\text{nonlinear}} = \frac{\lambda}{4\pi} G_r G_t \left(\frac{3}{2} c_3 a_2^2\right)^2. \tag{6}$$

Note from (5) that the linear RCS only depends on the scatterer itself whereas the nonlinear RCS in (6) depends on the scatterer properties as well as the signal level of the illuminator. In this fashion, having a strong illuminator allows for the nonlinear return to be sufficiently amplified to be detectable.

2.2.2 Computer Simulation

The nonlinear phantom used in this experiment was a model of a 1U rack-mount server, with external dimensions 50 cm by 80 cm. The case was modeled as a series of linear scatterers of approximate RCS equivalent to a metallic plate of the appropriate dimensions. The internals were modeled as 20 nonlinear scatterers uniformly distributed in space with $c_1 = 1$, $c_3 = -0.145$, $G_t = G_r = 0.1$ and a PCB transmission line impedance of $Z_0 = 100\ \Omega$. The images were computed using a standoff distance of 1.4 m from the centroid of the target using a CPI of 2^{22} pulses.

The pulse only, pulse + illuminator, and contrast images for this experiment are shown in Figure 1. It can be seen that the approximate locations of the strongest scatterers are clearly visible. It is not expected that the contrast image will reveal detailed schematic-level information due to the waveform range resolution, which is approximately 7.5 cm. Still, this may be enough for a sufficiently sophisticated ML algorithm to detect a difference.

2.3 Cyclostationary Feature Detection

2.3.1 Theory

If we discretize the received signal $y(t)$ using sample period Δ and denote it $Y[n]$, i.e.

$$Y[n] = y(n\Delta) \tag{7}$$

we can define the instantaneous autocorrelation function (ACF) $\mathscr{R}_{2Y}[n, \tau]$ as

$$\mathscr{R}_{2Y}[n, \tau] = \mathbb{E}\left[Y[n + \beta\tau]Y^*[n - \bar{\beta}\tau]\right], \tag{8}$$

where $\beta \in [0, 1]$ such that $\beta + \bar{\beta} = 1$ is a parameter used to generalize the definition to include differing conventions for the ACF used across the literature [32]. (In this work we will use $\beta = 1/2$.) If we take the Fourier transform with respect to τ, we obtain the Wigner-Ville spectrum (WVS), denoted $\mathscr{WV}_{2Y}$, i.e.

$$\mathscr{WV}_{2Y}[n, f) = \Delta \sum_{\tau=-\infty}^{\infty} \mathscr{R}_{2Y}[n, \tau]e^{-j2\pi f\tau\Delta}, \tag{9}$$

which can be interpreted as a time-varying power-spectrum. The ability to quantify the time-varying nature of the power spectrum of $Y[n]$ is necessary In the case where the WVS is periodic in n with one or more discrete frequency components (called cycle frequencies) from the set $\mathscr{A} = \{\alpha_i\}$, we say that the random process $Y[n]$ is a second-order cyclostationary (CS) signal.

An example of a second-order CS signal is given in Figure 2, which is a time domain capture of conducted electromagnetic interference (EMI) from a fluorescent light fixture, collected for the Flaming Moe dataset [33]. In the time domain it can be seen that the signal modulation appears somewhat random yet it has periodic fluctuations approximately every $1/120 = 8.33$ ms, which corresponds to the positive and negative peaks of the 60 Hz AC power signal. This behavior is also visible in the spectrogram, shown in Figure 3, which is an estimator of the WVS, where it can be seen that a spectral component at a frequency of approximately 2.5 kHz is modulated with a period of approximately 8.33 ms. In this case $\alpha = 120$ Hz would clearly be a cycle frequency of this signal.

The spectral correlation (SC) is defined as

$$\mathscr{SC}_{2Y}(\alpha, f) = \Delta \sum_{n=-\infty}^{\infty} \mathscr{WV}_{2Y}[n, f)e^{-j2\pi\alpha n\Delta}, \tag{10}$$

which can be interpreted as a bi-frequency spectrum that characterizes the nonstationary behavior of $Y[n]$, where α is the cycle frequency and f is ordinary frequency.

In the case when $Y[n]$ is a second-order CS signal, the SC contains discrete spectral lines at the α_i frequencies, i.e.

$$\mathscr{SC}_{2Y}(\alpha, f) = \sum_{\alpha_i \in \mathscr{A}} \mathscr{S}_{2Y}(f; \alpha_i)\delta(\alpha - \alpha_i), \tag{11}$$

where $\mathscr{S}_{2Y}(f; \alpha_i)$ is known as the cyclic power spectrum. It can be shown that the cyclic power spectrum is equivalent to

$$\mathscr{S}_{2Y}(f; \alpha_i) = \lim_{L\to\infty} \frac{1}{L\Delta}\mathbb{E}\left[Y_L(f + \alpha_i/2)Y_L^*(f - \alpha_i/2)\right], \tag{12}$$

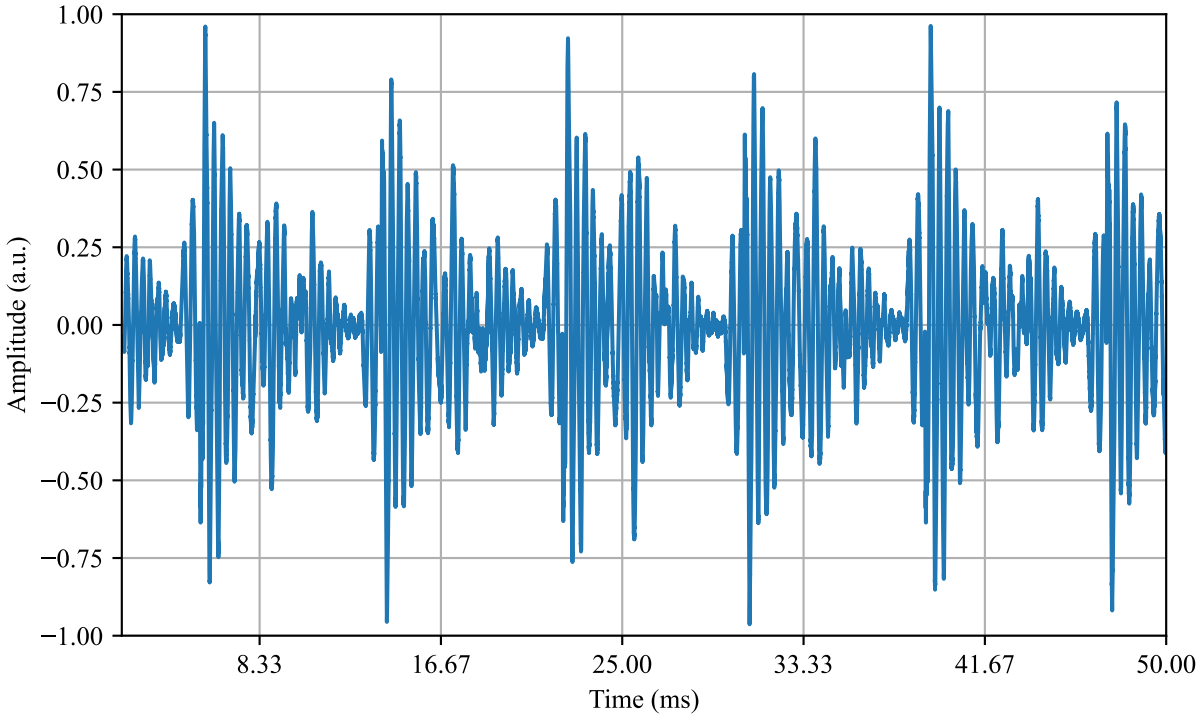

Figure 2. Time domain measurement of conducted EMI from fluorescent lights.

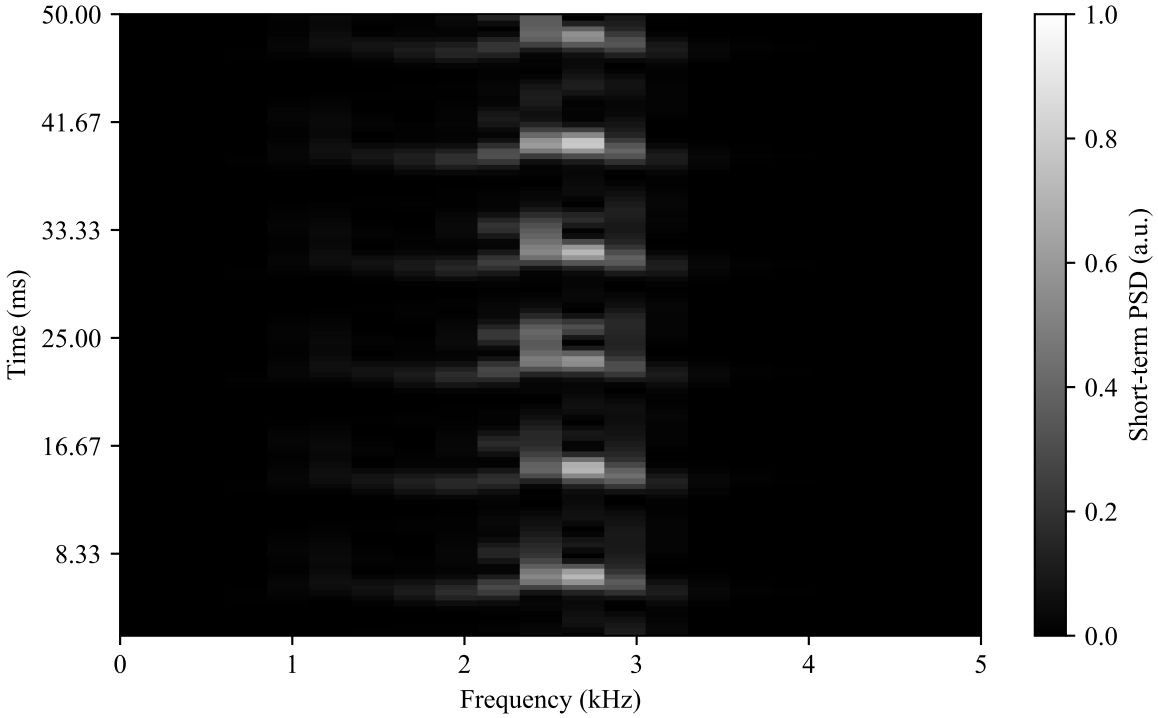

Figure 3. Spectrogram of conducted EMI from fluorescent lights.

where $Y_L(f) = \Delta \sum_{n=0}^{L-1} Y[n]e^{-j2\pi fn\Delta}$ is the L-point discrete-time Fourier transform (DTFT) of $Y[n]$. The form of (12) implies that the cyclic power spectrum, and by extension, the SC, can be estimated for a CS signal using any standard estimator for the cross-spectral density between frequency-shifted versions of $Y[n]$ separated by offset α_i.

In the case when $\alpha_i = 0$, the cyclic power spectrum reduces to the ordinary power spectrum $\mathscr{S}_{2Y}(f)$, i.e.

$$\mathscr{S}_{2Y}(f;0) = \mathscr{S}_{2Y}(f). \tag{13}$$

If we define

$$Y_-[n] = Y[n]e^{-j\pi\alpha n\Delta} \tag{14}$$

$$Y_+[n] = Y[n]e^{j\pi\alpha n\Delta} \tag{15}$$

we can define a normalized SC function called the cyclic coherence function that functions as a correlation coefficient. The cyclic coherence function γ_{2Y} is defined by

$$\gamma_{2Y}(f;\alpha) = \frac{\mathscr{S}_{2Y}(\alpha, f)}{\sqrt{\mathscr{S}_{2Y_-}(f)\mathscr{S}_{2Y_+}(f)}} \tag{16}$$

which, similar to a traditional correlation coefficient, lies in the range $0 \leq |\gamma_{2Y}|^2 \leq 1$. The magnitude-squared cyclic coherence (MSCC) can be used as a measure of statistical significance to determine the "strength" of a cyclostationary component, and thus is suitable for use as a detection statistic.

2.3.2 Application to Device Discrimination

As has been observed from analysis of the Flaming Moe data [15], emissions from device power supplies provide a means for uniquely identifying a device class. As well, in [14] it was seen that even within the same device class, device to device variations were observable. These measurement campaigns, however, used a line filter that was plugged directly into the power circuit adjacent to the DUT to measure conducted emissions.

It would be more convenient for a technician to be able to sense these fluctuations without requiring physical contact with the DUT or power circuit. Using a similar physical principle as in Section 2.2, a UWB radar could theoretically be used to probe a DUT, where intermodulation of the power supply emissions with the radar pulses is then backscattered to the radar receiver. CS signal analysis techniques would then be used to identify the source of the emissions.

We will denote the received signal from the pulsed UWB radar as $Y_m[n]$, where m is the range bin along the "fast time" dimension and n is the time index along the "slow time" or pulse repetition interval (PRI) dimension [34]. To detect the presence of CS signal components in the received signal, we can compute the MSCC $|\gamma_{2Y_m}(f;\alpha)|^2$ for each range bin m.

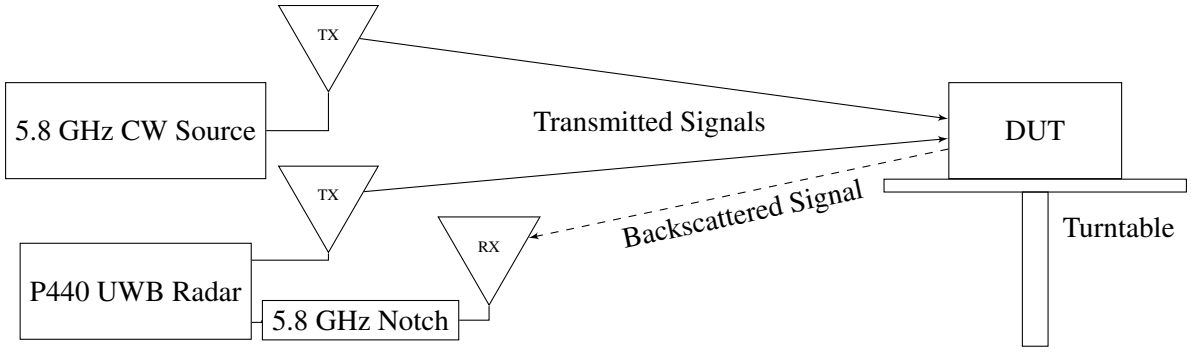

Figure 4. System diagram.

3 EXPERIMENTAL SETUP

In this work, we propose the application of a known IR-UWB IMOD approach using an external illuminator [28] to this specific problem. A system diagram is shown in Figure 4. The system consists of a TDSR P440 UWB radar with approximately 2 GHz bandwidth for high downrange resolution with the device under test (DUT) placed on a rotating turntable to enable a 360° view of the target so that tomographic processing can be performed [35]. To generate nonlinear IMOD components, an OOB CW 5.8 GHz source is used to illuminate the target. Tomographic imaging will be performed on the nonlinear component of the return signal, allowing for a 2D image to be generated which can be used to differentiate between devices.

To validate that our tomographic imaging system was functioning properly, we constructed a calibration target consisting of metallic cans (which are known to have a large linear RCS) in known locations. A picture of the target is shown in Figure 5. The tomography image generated (using linear imaging only) is shown in Figure 6. To generate this image, the 1-D radar returns at each angle were collected into a matrix to form the sinogram. The radar return generated by the UWB radar was the real-valued RF signal; to remove the effect of the carrier frequency we took the Hilbert transform to compute the signal envelope (denoted by the "method=env" figure annotation). The inverse Radon transform was then applied to the sinogram to generate the tomography image. The location of the four cans can clearly be seen from this figure.

Figure 5. Calibration target.

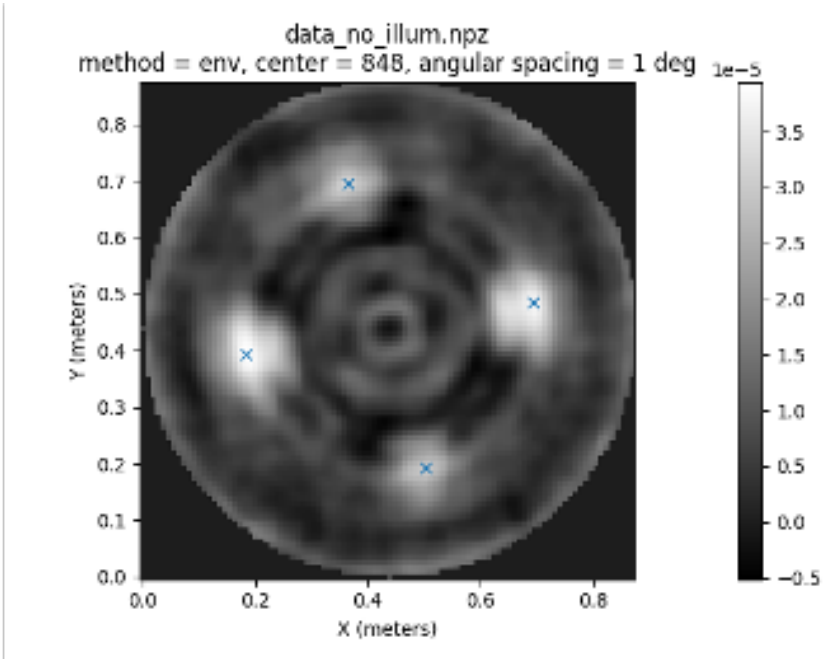

Figure 6. Tomography image generated from calibration target.

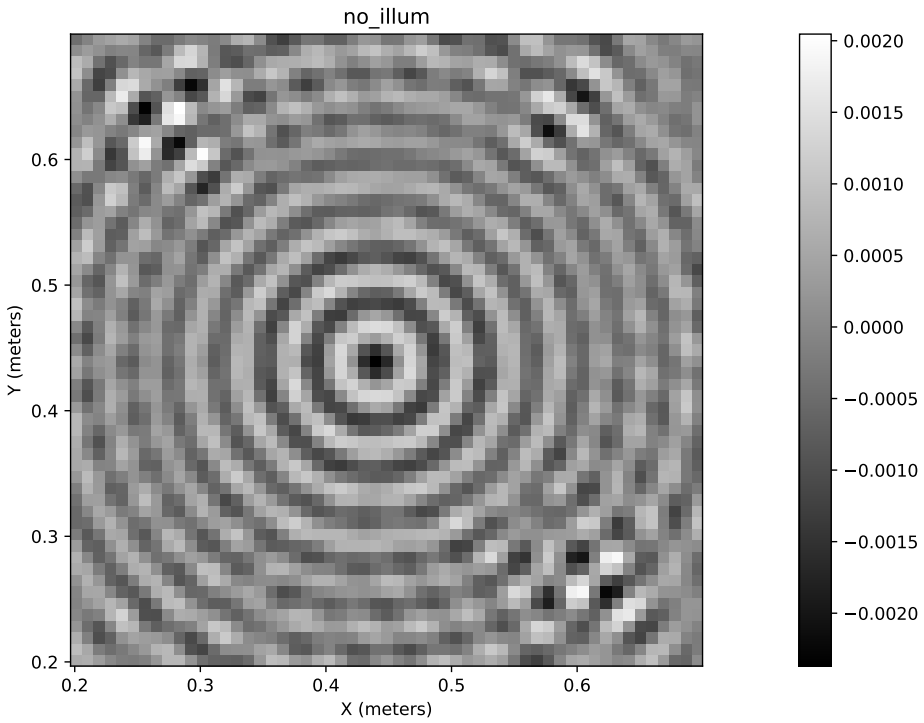

Figure 7. No illuminator present.

4 RESULTS

To attempt to detect the presence of a device containing nonlinear electronics, we devised an experiment wherein we used the aforementioned calibration target as the basis for imaging but removed one of the cans and placed a DUT at that location. In this case we chose to use a USRP B210 software defined radio (SDR) without the metallic enclosure, so the configuration consisted of the SDR printed circuit board (PCB) supported by metallic standoffs. The SDR had antennas attached to transmit and receive ports. This DUT was chosen because the RF front-end should provide a natural conductive path for the radar waves to propagate and excite the electronic internals. In other words, this target should be one of the easiest devices to detect.

A tomographic image was generated for both the with and without illumination cases. In this case we chose to form the sinogram using the real RF signal (rather than the envelope computed from the Hilbert transform). These images are shown in Figures 7-9. The data was collected in 5 degree increments, and at each angle $16773120 \approx 2^{24}$ pulses were coherently integrated to reduce noise. The radar's effective PRF is approximately 1.25 MHz, so the data collection for these images took several minutes.

In the tomography images the location of the three remaining cans can clearly be seen; however there does not appear to be a strong return at the DUT location, either in the linear return or in the contrast.

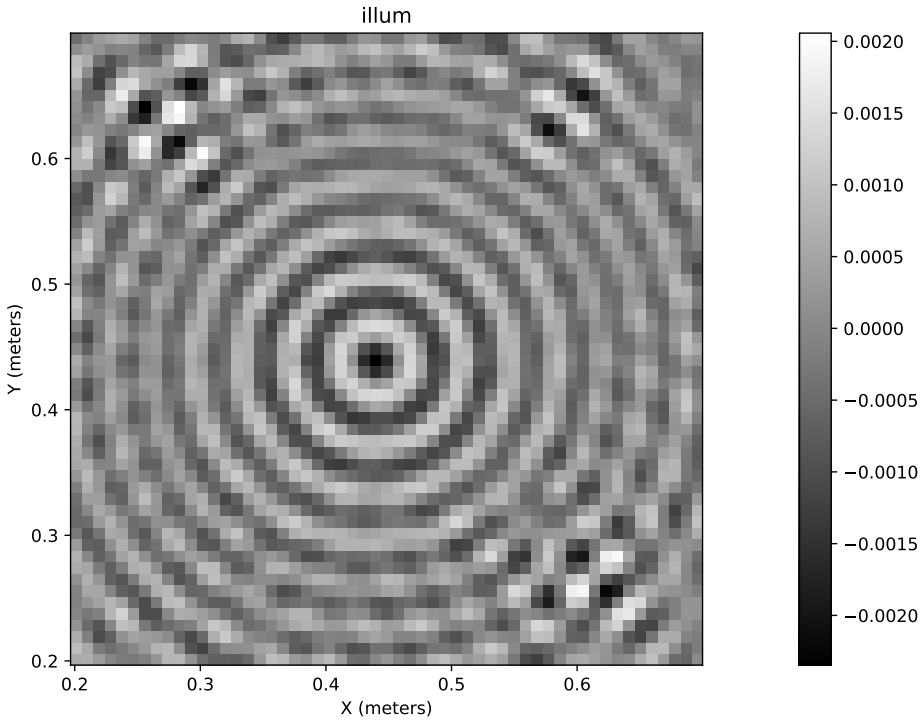

Figure 8. Illuminator present.

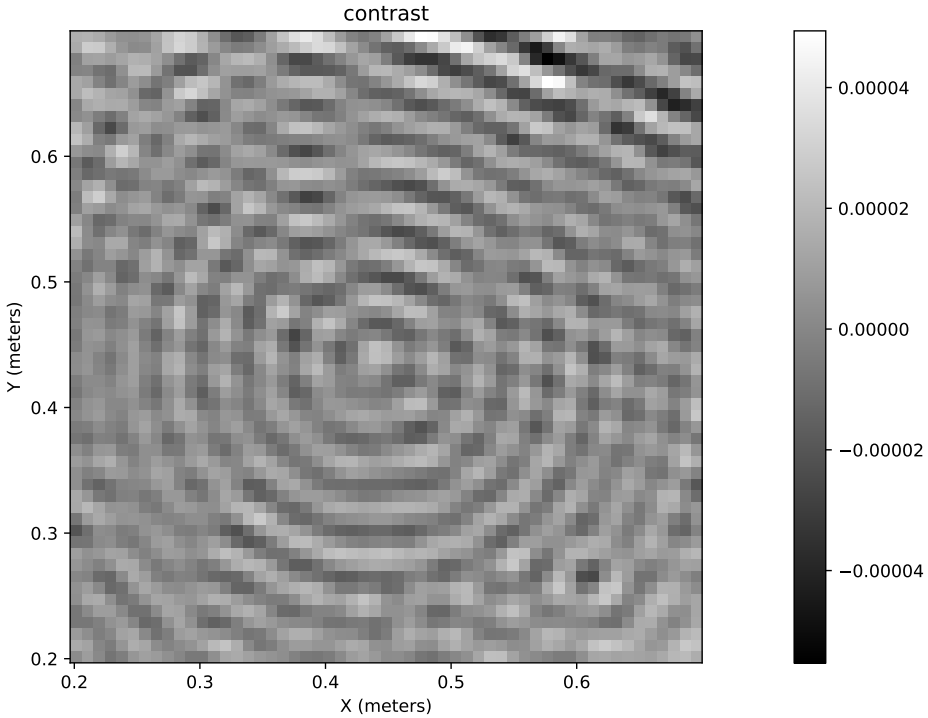

Figure 9. Contrast image.

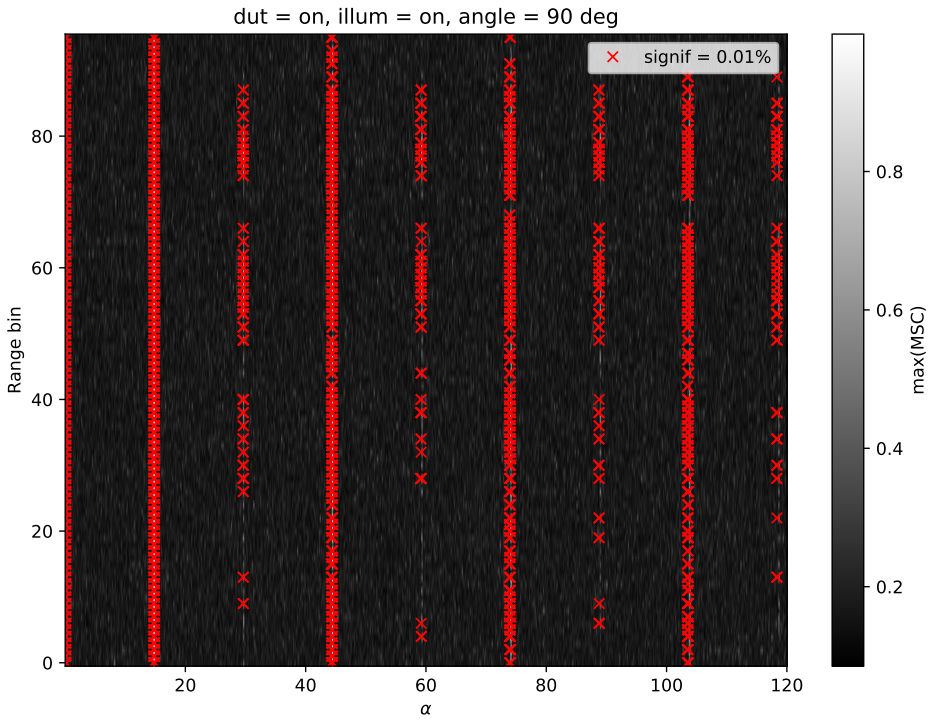

Figure 10. MSC of target with DUT powered on.

The MSC of this DUT was also computed from the radar returns collected during this experiment. To compute a useful image, we computed the MSC for each range bin across 65520 slow-time samples and took the maximum MSC value over f. The resulting output is a spectrum of cycle frequencies per range bin, the goal of which is to identify cyclic spectral components as a function of range at a single observation angle. The resulting image is shown in Figure 10. Cyclic components are visible at multiples of 14.7 Hz. Initially it was thought that this could have been generated by the DUT, but this signal was observed in every test we performed (even without this DUT), so we believe it may have been a signal generated in the radar receiver or conducted into the chamber through the power circuitry (it is not clear which is the source).

5 CONCLUSIONS

In this report we have described the principle of operation of a potential hardware implant and counterfeit device detector. Analytical and computer simulations have been shown to demonstrate a proof of concept; however our experimental results did not show a clear detection of our device under test even under the most favorable conditions.

We still cannot conclusively say that this method is infeasible, however. One reason is because the UWB radar we used, the TDSR P440, has a very low quantization resolution in the receiver analog to digital converter (5 bits). It attempts to overcome this limitation via a large PRF and coherent integration, but the signals we are concerned with may be too small even to toggle the least significant bit enough times to be "integrated out". A higher fidelty receiver and analog to digital converter may resolve this issue, but it is uncertain.

6 REFERENCES

References

[1] 2017 Public-Private Analytic Exchange Program (AEP), "Supply chain risks of SCADA/industrial control systems in the electricity sector: Recognizing risks and recommended mitigation actions," Office of the Director of National Intelligence, Tech. Rep., 2017, https://www.odni.gov/files/PE/Documents/11---Supply-Chain-Risks-of-SCADA-Industrial-Control-Systems-in-the-Electricity-Sector_Risks-and-Mitigations.pdf.

[2] J. Boyens, C. Paulsen, R. Moorthy, and N. Bartol, "Supply chain risk management practices for federal information systems and organizations," National Institute of Standards and Technology, Tech. Rep. NIST SP 800-161, April 2015, https://csrc.nist.gov/publications/detail/sp/800-161/final.

[3] Y. Hou, J. Such, and A. Rashid, "Understanding security requirements for industrial control system supply chains," in *2019 IEEE/ACM 5th International Workshop on Software Engineering for Smart Cyber-Physical Systems (SEsCPS)*. IEEE, 2019, pp. 50–53.

[4] S. Yousuf and D. Svetinovic, "Blockchain technology in supply chain management: Preliminary study," in *2019 Sixth International Conference on Internet of Things: Systems, Management and Security (IOTSMS)*. IEEE, 2019, pp. 537–538.

[5] R. S. Gaonkar and N. Viswanadham, "Analytical framework for the management of risk in supply chains," *IEEE Transactions on automation science and engineering*, vol. 4, no. 2, pp. 265–273, 2007.

[6] N. Alzahrani and N. Bulusu, "Block-supply chain: A new anti-counterfeiting supply chain using NFC and blockchain," in *Proceedings of the 1st Workshop on Cryptocurrencies and Blockchains for Distributed Systems*, 2018, pp. 30–35.

[7] O. Duman, M. Ghafouri, M. Kassouf, R. Atallah, L. Wang, and M. Debbabi, "Modeling supply chain attacks in IEC 61850 substations," in *2019 IEEE International Conference on Communications, Control, and Computing Technologies for Smart Grids (SmartGridComm)*. IEEE, 2019, pp. 1–6.

[8] S. Boyson, "Cyber supply chain risk management: Revolutionizing the strategic control of critical IT systems," *Technovation*, vol. 34, no. 7, pp. 342–353, 2014.

[9] D. Forte, R. Perez, Y. Kim, and S. Bhunia, "Supply-chain security for cyberinfrastructure [guest editors' introduction]," *Computer*, vol. 49, no. 8, pp. 12–16, 2016.

[10] D. Inserra and S. P. Bucci, "Cyber supply chain security: A crucial step toward US security, prosperity, and freedom in cyberspace," *The Heritage Foundation, Backgrounder*, no. 2880, p. 8, 2014.

[11] A. Yeboah-Ofori, S. Islam, and A. Brimicombe, "Detecting cyber supply chain attacks on cyber physical systems using Bayesian belief network," in *2019 International Conference on Cyber Security and Internet of Things (ICSIoT)*. IEEE, 2019, pp. 37–42.

[12] Q. Huang, X. Li, C. Fang, F. Yang, Y. Su, and X. Zeng, "An aggregating based model order reduction method for power grids," *Integration*, vol. 55, pp. 449–454, 2016.

[13] J. F. Miller, "Supply chain attack framework and attack patterns," MITRE Corp, Tech. Rep. MTR140021, 2013.

[14] C. D. Cooke, F. K. Reed, L. J. Prince, J. M. Vann, and A. L. Anderson, "An efficient sparse FFT algorithm with application to signal source separation and 2D virtual image feature extraction," in *MILCOM 2016-2016 IEEE Military Communications Conference*. IEEE, 2016, pp. 396–400.

[15] J. M. Vann, T. P. Karnowski, R. Kerekes, C. D. Cooke, and A. L. Anderson, "A dimensionally aligned signal projection for classification of unintended radiated emissions," *IEEE Transactions on Electromagnetic Compatibility*, vol. 60, no. 1, pp. 122–131, 2017.

[16] G. J. Mazzaro, A. F. Martone, K. I. Ranney, and R. M. Narayanan, "Nonlinear radar for finding RF electronics: System design and recent advancements," *IEEE Transactions on Microwave Theory and Techniques*, vol. 65, no. 5, pp. 1716–1726, 2017.

[17] G. J. Mazzaro, A. F. Martone, and D. M. McNamara, "Detection of RF electronics by multitone harmonic radar," *IEEE Transactions on Aerospace and Electronic Systems*, vol. 50, no. 1, pp. 477–490, 2014.

[18] K. Ranney, K. Gallagher, A. Martone, G. Mazzaro, K. Sherbondy, and R. Narayanan, "Instantaneous, stepped-frequency, nonlinear radar," in *Radar Sensor Technology XIX; and Active and Passive Signatures VI*, vol. 9461. International Society for Optics and Photonics, 2015, p. 946122.

[19] K. Ranney, G. Mazzaro, K. Gallagher, A. Martone, K. Sherbondy, and R. Narayanan, "Instantaneous stepped-frequency, non-linear radar part 2: experimental confirmation," in *Radar Sensor Technology XX*, vol. 9829. International Society for Optics and Photonics, 2016, p. 98291P.

[20] J. Owen, S. D. Blunt, K. Gallagher, P. McCormick, C. Allen, and K. Sherbondy, "Nonlinear radar via intermodulation of FM noise waveform pairs," in *2018 IEEE Radar Conference (RadarConf18)*. IEEE, 2018, pp. 0951–0956.

[21] J. Owen, C. Mohr, S. D. Blunt, and K. Gallagher, "Nonlinear radar via intermodulation of jointly optimized FM noise waveform pairs," in *2019 IEEE Radar Conference (RadarConf)*. IEEE, 2019, pp. 1–6.

[22] J. Raoult, A. Martorell, L. Chusseau, and C. Carel, "Intermodulation radar for RF receiver detections," in *2018 15th European Radar Conference (EuRAD)*. IEEE, 2018, pp. 273–276.

[23] A. Martorell, J. Raoult, L. Chusseau, and C. Carel, "Compact intermodulation radar for finding RF receivers," in *2019 16th European Radar Conference (EuRAD)*. IEEE, 2019, pp. 109–112.

[24] K. A. Gallagher, G. J. Mazzaro, K. I. Ranney, L. H. Nguyen, A. F. Martone, K. D. Sherbondy, and R. M. Narayanan, "Nonlinear synthetic aperture radar imaging using a harmonic radar," in *Radar Sensor Technology XIX; and Active and Passive Signatures VI*, vol. 9461. International Society for Optics and Photonics, 2015, p. 946109.

[25] K. A. Gallagher, R. M. Narayanan, G. J. Mazzaro, A. F. Martone, and K. D. Sherbondy, "Static and moving target imaging using harmonic radar," *Electronics*, vol. 6, no. 2, p. 30, 2017.

[26] H. T. Hayvaci, H. Ilbegi, and I. S. Yetik, "Classification of electronic devices with power-swept signals using harmonic radar," *IEEE Transactions on Aerospace and Electronic Systems*, vol. 56, no. 3, pp. 2292–2301, 2019.

[27] J. Park and S. H. Cho, "IR-UWB radar sensor for human gesture recognition by using machine learning," in *2016 IEEE 18th International Conference on High Performance Computing and Communications; IEEE 14th International Conference on Smart City; IEEE 2nd International Conference on Data Science and Systems (HPCC/SmartCity/DSS)*. IEEE, 2016, pp. 1246–1249.

[28] V. P. Yakubov, S. Shipilov, R. Satarov, and A. V. Yurchenko, "Remote ultra-wideband tomography of nonlinear electronic components," *Technical Physics*, vol. 60, no. 2, pp. 279–282, 2015.

[29] N. Blaunstein and V. Yakubov, *Electromagnetic and Acoustic Wave Tomography: Direct and Inverse Problems in Practical Applications*. CRC Press, 2018.

[30] A. C. Kak and M. Slaney, *Principles of computerized tomographic imaging*. IEEE Press, 1988.

[31] C. D. Cooke, "Behavioral amplifier modeling for radar simulation with application to nonlinear effects of multiple impinging signals," in *2017 IEEE Radar Conference (RadarConf)*. IEEE, 2017, pp. 0308–0313.

[32] J. Antoni, "Cyclic spectral analysis in practice," *Mechanical Systems and Signal Processing*, vol. 21, no. 2, pp. 597–630, Feb. 2007. [Online]. Available: https://www.sciencedirect.com/science/article/pii/S0888327006001816

[33] T. Karnowski, R. Kerekes, C. Cooke, M. Vann, M. Adams, and P. Bingham. (2021, September) Flaming Moe. [Online]. Available: https://www.osti.gov/biblio/1784765

[34] M. A. Richards, *Fundamentals of Radar Signal Processing*, 2nd ed. McGraw Hill, 2014.

[35] R. W. Deming, "Tutorial on Fourier space coverage for scattering experiments, with application to SAR," in *Algorithms for Synthetic Aperture Radar Imagery XVII*, vol. 7699. International Society for Optics and Photonics, 2010, p. 769904.